Ocean Engineering 332 (2025) 121419

Contents lists available at ScienceDirect

Ocean Engineering

journal homepage: www.elsevier.com/locate/oceaneng

Research paper

# Downstream tidal turbine transient local blade loading characterization

Vincent Podeur [a,b], Lise Michaud [b], Dominic Groulx [b,*], Christian Jochum [a]

[a] Institut de Recherche Dupuy de Lôme (IRDL), ENSTA Bretagne / IRDL-UMR CNRS 6027 Brest Cedex 09, F-29806, France
[b] Department of Mechanical Engineering, Dalhousie University, Halifax, Nova Scotia, B3H 4R2, Canada

ARTICLE INFO

*Keywords:*
Horizontal axis tidal turbine (HATT)
Transient blade loading
Turbine interaction
RANS-SST
Transient CFD

ABSTRACT

Flow perturbations carried in the wake of an upstream turbine can have a significant impact on the local and transient loads observed on the downstream one. To get a better understanding of the effect of unsteady asymmetric flow on the load felt by a downstream turbine and develop a method to extract local and transient blade loading from CFD results, fully transient simulations designed to study this effect were performed with a RANS $k$-$\omega$ SST turbulence model using ANSYS-CFX. A horizontal axis tidal turbine (HATT) was used for the study. Three configurations were considered: the downstream turbine aligned with the upstream one, the downstream turbine offset by 0.5$D$ and finally offset by 1$D$, with $D$ being the diameter of the turbine. A 10$D$ clearance between both turbines was used. Results show that when fully in-line, the downstream turbine sees reduction in power coefficient by almost 70 %, with a temporal variation of this coefficient having a relative amplitude of more than 30 %. Furthermore, the blades see localized loading varying by a factor of up to 2 during their rotation and the changes in the load amplitude applied at the same location are varying by more than 13 %. Blade load and flap-wise bending moment display significant amplitude variations for the 0$D$ and 0.5$D$ offsets, with values 8 and 12 times higher to what is observed for the 1$D$ offset.

Nomenclature

| Symbol | Name | Unites |
|---|---|---|
| $\omega$ | rotational speed | rad/s |
| $\rho$ | water density | 997 $kg/m^3$ |
| $A$ | turbine swept area | $m^2$ |
| $A_b$ | single blade surface area | $m^2$ |
| $A_s$ | $n$th blade section's area | $m^2$ |
| $C_M$ | flap-wise root bending moment coefficient | [-] |
| $C_p$ | power coefficient | [-] |
| $C_t$ | thrust coefficient | [-] |
| $C_{tl}$ | local thrust coefficient | [-] |
| $D$ | turbine diameter | m |
| $M$ | flap-wise root bending moment | Nm |
| $P$ | power | W |
| $P_{rel}$ | relative pressure | Pa |
| $Q$ | torque | Nm |
| $R_O$ | reference frame | [-] |
| $T$ | thrust | N |
| $T_l$ | local thrust of the nth blade section | N |
| TSR | tip speed ratio | [-] |
| $U_0$ | inlet flow velocity | m/s |
| $\vec{x}, \vec{y}, \vec{z}$ | unit vectors attached to R0 | m |
| ***Acronym*** | ***Meaning*** | |

(*continued on next column*)

(*continued*)

| | |
|---|---|
| BEMT | Blade Element Momentum Theory |
| CFD | Computational Fluid Dynamics |
| DES | Detached Eddy Simulations |
| EMEC | European Marine Energy Centre Ltd |
| FORCE | Ocean Research Centre for Energy |
| GCI | Grid Convergence Index |
| HATT | Horizontal Axis Tidal Turbine |
| IFS | Fluid-Structure Interaction |
| LES | Large Eddy Simulation |
| LES-ALM | Large Eddy Simulation-Actuator Line Method |
| RANS | Reynolds Averaged Navier Stokes |
| RMS | Root Mean Square |
| TI | Turbulence Intensity |
| GGI | General Grid Interface |

## 1. Introduction

While writing this introduction in July 2023, Europe is seeing the highest temperatures ever recorded, Asia and North America are also dealing with important heat waves; all consequences of climate change. The price of oil and gasoline at the pump are also seeing record highs. These extreme environmental and economic situations are furthering

* Corresponding author.
*E-mail address:* dominic.groulx@dal.ca (D. Groulx).

https://doi.org/10.1016/j.oceaneng.2025.121419
Received 19 July 2024; Received in revised form 5 December 2024; Accepted 28 April 2025
Available online 10 May 2025

the need and commitment to greener, sustainable and renewable practices, including in the production of energy. Tidal energy has been a subject of increased research and development, both in the academia and industry for nearly two decades. Tidal turbines have been designed and tested at various demonstration sites, the European Marine Energy Centre Ltd (EMEC) in Scotland or the Fundy Ocean Research Centre for Energy (FORCE) site in Nova Scotia, Canada; to name a few. However, due to the harsher conditions tidal turbines have to operate in, few newer tidal turbines have been put in grid-connected operations since, pointing to complexities and unanswered questions related to their designs, constructions, operations, maintenance as well as regulatory and environmental impacts.

This harsher environment puts a lot of constrain regarding the design of tidal turbines and their implantation. One constrains of particular interest is the space limitation imposed by the topology of the local bathymetry. Contrary to what can be observed in the wind turbine industry, designer may not be able to position their turbines exactly the way they want, especially in the context of tidal turbine farms (Topper et al., 2021; Patel, 2024).

Installing an array of turbines in such coastal area requires some key factors to be taken into account such as the impact of the array on the local wildlife (Patel, 2024; Hammar et al., 2013; Onoufriou et al., 2021), on the hydrodynamics of the local flow (du Feu et al., 2019; Zhang et al., 2022), on sediment transport (Fairley et al., 2015) or its effect on local human activities. In addition to these limiting factors, operational and financial constrains should also be considered when designing a tidal array layout, in order to reduce maintenance and installation costs (Roc et al., 2013).

In this context, two or more turbines may be installed in close proximity. This confinement is leading to unavoidable interactions between upstream turbines' wakes and downstream turbines (Bai et al., 2013). The velocity deficit in conjunction with the increase of the flow turbulence will influence the performance of the downstream turbine. Moreover, a downstream turbine situated partially in the wake of an upstream one would be exposed to an asymmetric flow which will induce asymmetric load on turbine blades.

As shown experimentally by Jeffcoate et al. (2016), the high turbulence level of the incoming flow on a turbine has a significant impact on turbine performances, leading to a decrease of up to 63 % of its performance (spacing between the turbines from $2D$ to $6D$). This figure highlights the fact that perturbations carried in the wake of an upstream turbine may also be of significant impact on the downstream one. This problematic has already been addressed numerically but with simplified approaches such as the Blade Element Momentum Theory (BEMT) often coupled with a RANS CFD approach (Masters et al., 2013; Turnock et al., 2011). These studies give interesting results regarding power extraction but as expressed in (Leroux et al., 2016, 2019), lack some precision regarding definition of the structure of the wake and its effect on load variation on the turbine blades. More recent work combining a BEMT approach with detached eddy simulations (DES) concluded that both power production and thrust on backrow turbines have considerably more temporal variability, pointing to potential implications related to device wear and fatigue (Gajardo et al., 2019). Loads on turbines within an array were also studied numerically using a large eddy simulation-actuator line method (LES-ALM) approach (Ouro et al., 2019). The authors concluded that the turbines in the front row saw the largest thrust loads and blade root bending moments, while the back-row turbines experienced the largest yaw moments due to their exposures to low momentum wakes and high-velocity free streams.

Experimentally, Mycek et al. (2014) studied the interaction of two in-line turbines as a function of their spacing in a flume tank. Results showed that at low turbulence intensity (TI), the thrust on the downstream turbine was always lower compared to the thrust on a single one; at higher TI, the downstream thrust could reach the same level as that on a single turbine. However, the fluctuation of the downstream thrust was determined to be three times larger at low TI. As part of an experimental campaign, Allmark et al. (2021) tested a configuration with two turbines, in line with each other or offset by one diameter of the upstream turbine and separated by 7 diameters of the upstream turbine (upstream turbine diameter of 0.5 m, downstream turbine diameter of 0.9 m). The thrust coefficient on the downstream in-line turbine increased by up to 25 % while the root bending moments remained similar compared to the single turbine case (Allmark et al., 2021).

Recent research work has also focused on the measure (experimental) or determination (numerical) of loads on turbine blades due to turbulent tidal flow recognizing that it is detrimental to the fatigue life of the turbine (Blackmore et al., 2016). Milne et al. (2015) experimentally measured thrust and bending moments on a turbine blade subjected to unsteady (oscillatory frequency) flow; transient variations of up to 40 % in bending moment were observed. Blackmore et al. (2016) determined that turbine thrust could vary by up to 20 % and bending moments by up to 80 % during their experimental trial where the impact of turbulence intensity and integral length were studied. Payne et al. (2018) looked at loads on both the turbine blades and the turbine tower in relation to turbulent flow frequency and spectra. Lloyd et al. (2021) studied the impact of the tidal vertical velocity profile as well as current-wave interaction and determined that transient thrust experienced greater variation for a profiled current-only conditions compared to a uniform flow. Waves further increased the amplitude of thrust and torque fluctuations by 35 times the current-only cases. Similar conclusions on the impact of vertical velocity profiles were found experimentally in (Zhang et al., 2023; Magnier et al., 2022) and numerically in (Guy et al., 2024).

Various numerical approaches have also been used to determined transient load changes on turbine and turbine blades. A Reynolds Averaged Navier Stokes (RANS) $k$-$\omega$ Shear Stress Transport (SST) is the most common computational fluid dynamics (CFD) method used. Afgan et al. (2013) used it, and compared it to an LES approach, to determine the overall turbine load fluctuation subjected to a steady constant inlet flow; with the LES results predicting larger fluctuations. This CFD method was coupled with a finite element method to perform Fluid-Structure Interaction (FSI) studies looking at the effect of wave-current interactions on a turbine in (Tatum et al., 2016). Again, the researchers determined that blade and turbine loading would fluctuate, the wave having the greatest impact on the fluctuation amplitude. Large eddy simulation (LES) was also used in addition to RANS $k$-$\omega$ SST in (Ahmed et al., 2017) to determine turbine load and blade root bending moments for a device subjected to a velocity profile typically found at EMEC; again, obtaining important fluctuations as a function of the rotational positions of the blades in the flow. Finnegan et al. (2020) focused on fatigue loading of turbine blades by numerically solving for a mean tidal flow measured at Pentland Firth also using a RANS $k$-$\omega$ SST approach and including the impact of the support structure. It was determined that thrust forces on the blades could vary by up to 43 % during their rotation.

Using an unsteady BEMT approach, Nevalainen et al. (2016) studied the impact of numerous parameters related to the tidal flow/sea-state, turbine operational domain and geometry would have on the turbine operation and load. They determined that for a given flow, loads could vary greatly in magnitude and angular distribution. Even when the mean amplitude of the loads did not vary significantly, the fluctuations around the mean value could have a large impact on the drivetrain components fatigue. Togneri et al. (2020) also used BEMT to determine the impact of TI on the overall turbine load fluctuations, concluding that fluctuations increase with TI. Various strategies have also been looked at experimentally to reduce the amplitude and impact of load variations. Liu et al. (2020) looked at pitch-control of blades to reduce asymmetric loads during the sea trial of a 600-kW two-bladed horizontal axis tidal turbine (HATT). Porter et al. (2020) tested passively adaptive composite blades under current and wave loading finding that the thrust and torque fluctuation magnitudes per cycle were reduced by 10 and 14 % respectively compared to aluminum blades.

**Table 1**
Turbine dimensions.

| Parameter | Dimension |
|---|---|
| Turbine diameter $D$ | 0.762 m |
| Hub diameter | 0.15 m |
| Rotor depth | 1.25 m |
| Nacelle length | 1.70 m |

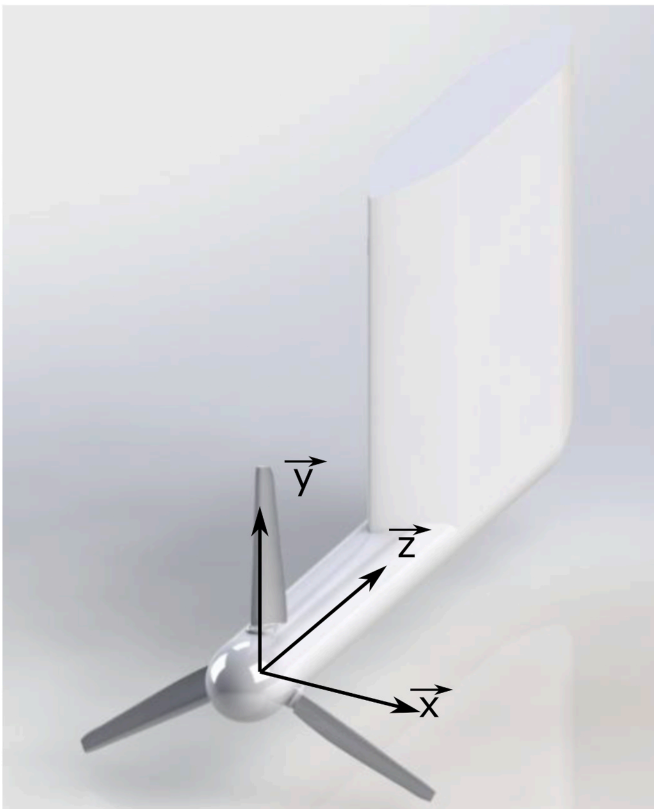


**Fig. 1.** 3D rendering of the turbine and its nacelle.

Despite extensive literature review, there remains a lack of understanding of the effect of unsteady asymmetric wake flow on a downstream turbine, especially regarding local blade load variation. A better understanding of the hydrodynamic load variation due to the incoming wake will provide valuable information for the industrial ecosystem to improve tidal turbine technology readiness levels. Unfortunately, experimental measurements have limitations in the level of detail they can achieve for blade load measurement. The literature review indicates that mainly integral quantities, such as power output or blade root bending moment, are available during flume tank test. As illustrated in (Munaweera Thanthirige et al., 2023), more advanced measurements can be conducted on a dry test bench using a full-scale blade. However, these tests are expensive and fail to replicate the blade load variations experienced during actual operation, hence leaving a gap in the structural design process (Munaweera Thanthirige et al., 2023). Failure to replicate real-life loading scenarios with full scale test bench is also mentioned by Lame (Lam et al., 2023), who highlights the fact that tidal turbines are subject to complex load variation induced by waves, which can lead to severe under prediction of fatigue damage if not considered. Obtaining local measurements of blade load variation would require developing a new experimental setup, which demands financial resources and test facilities that are not readily available to the authors. As highlighted by the previous literature review, CFD computation is a viable alternative to experimental measurement for gaining better insights into the effect of turbine wake on blade load variation.

Thus, the aim of this paper is to provide a detailed analysis of the effect of upstream wake on a downstream turbine by examining both integral and local quantities with a focus on providing a methodology to determine local transient forces on blades from transient 3D CFD simulations. This analysis is based on results obtained from fully transient simulations employing RANS turbulence physics. Based on work previously done at Dalhousie University, simulations were designed to study the effect of the wake of an upstream turbine on a downstream one. Three different configurations have been considered: i) a downstream turbine aligned with the upstream one, ii) a downstream turbine offset by half the turbine diameter (0.5$D$) with respect to the longitudinal axis on the right side of the upstream one, iii) a downstream turbine offset by 1$D$. For all three setups, a 10$D$ clearance between both turbines was chosen. Both offset and downstream clearance values are based on those provided in (Myers and Bahaj, 2012) and (Marsh et al., 2021). The model of turbine considered for this study is a horizontal axis tidal turbine (HATT).

This paper will first present the implementation of the numerical model and its validation. Then, the numerical results regarding the influence of the upstream wake on the downstream turbine performances will be presented with a special focus on the blade load variation over time and the asymmetric load over the swept area.

## 2. Turbine geometry

The HATT turbine considered in this study is the one used in (Doman et al., 2015) and tested at Strathclyde University. The general dimensions of the turbine are given in Table 1 with a 3D rendering of it presented in Fig. 1. The blades are based on an NREL S814 profile. Regarding the blade root, the initial design was simplified to facilitate the meshing process. A detailed description of the blade geometry can be found in (Doman et al., 2015), and will not be repeated here. Regarding the nacelle dimensions, they were estimated from this paper.

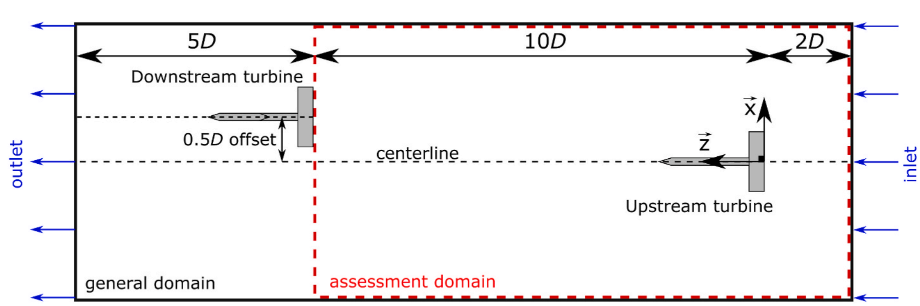


**Fig. 2.** Schematic representation of both numerical domains used in this study. The general domain contains two turbines and is used to study the wake to turbine interaction. The assessment domain contains one turbine and is used to assess the mesh quality.

**Table 2**
Boundaries conditions of the numerical domain.

| Boundary | Condition |
|---|---|
| Inlet | Steady normal flow: $U_0 = 1$ m/s |
| | Turbulence Intensity = 5 % |
| Outlet | Relative pressure $P_{rel} = 0$ Pa |
| Tank walls | Free slip, velocity at wall = $U_0$ |
| Turbine walls | No slip |
| Nacelle walls | No slip |

## 3. Numerical modeling

The numerical simulations presented in this study were performed using ANSYS CFX version 17.

### 3.1. Fluid domain and boundaries conditions

The general fluid domain considered for this study is based on the size of the Kelvin Hydrodynamics laboratory tow tank where the original turbine was tested. The width and depth of the channel are respectively 4.6 m and 2.5 m. The domain contains two turbines and has a total length of 17 turbine diameters ($D$). The reference frame $R_O(\vec{x}, \vec{y}, \vec{z})$ used in this study has its origin $O$ taken on the center line of the channel at $2D$ from the inlet, with $\vec{z}$ pointing in the same direction as the incoming flow and $\vec{y}$ pointing upward. The first turbine position, defined by the center of its hub, is located at $O$, the origin of the reference frame. The second turbine, called the downstream turbine, is at $10D$ on the $z$ axis. Its $y$ position is zero. For its $x$ position, three setups are considered. A first one where the turbine is aligned with the upstream one. A second one, with an offset of $0.5D$ on the $x$ axis, and a third one with an offset of $1D$. A schematic description of the domain is given in Fig. 2. Non-slip boundary conditions have been applied to the turbines and nacelles walls. For the sake of simplicity, free-slip conditions have been applied to the tank walls to mimic the movement of the turbine assembly in the tow tank. A full description of the boundaries conditions is given in Table 2.

From the diameter of the turbine and the cross-section of the testing channel, the blockage ratio for this study is 4.1 %. In 2015, Doman et al. commented that the blockage ratio at which to apply corrections is an on-going discussion (Doman et al., 2015). Since then, numerous previous studies have showed that blockage ratios under 5 % have very little effect on the turbine behaviour (Leroux et al., 2019; Osbourne, 2015). Badshah et al. looked at the impact of blockage ration and boundary proximity on the turbine performance and concluded that blockage ratio under 10 % had insignificant impact (Badshah et al., 2019).

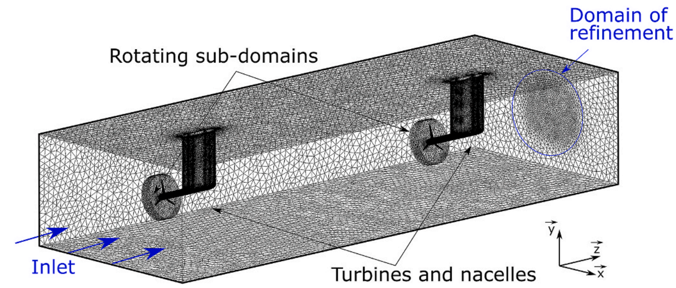


**Fig. 4.** Isometric view of the meshed general domain. The mesh refinement in the wake area is highlighted on the outlet of the domain.

Prior to studying the wake to turbine interaction, a smaller domain was considered to assess the quality of the meshing parameters and perform a validation. This was done to reduce the computational time. This domain, called assessment domain, had the same properties as the general one except for the part containing the downstream turbine being removed, as represented in Fig. 2.

### 3.2. Turbulence model

As reviewed in the introduction, more computationally expensive turbulence models, both Detached Eddy Simulations (DES) and Large Eddy Simulations (LES) could have been used in this work. However, with a stated goal of determining a method to extract CFD results in order to determine and present local and transient loads on turbine blade, it was decided to use a well known, reliable, and faster turbulence modeling approach. Therefore, because of the proven relevance of the results obtained in earlier works (Leroux et al., 2019; Afgan et al., 2013; Currie et al., 2016; Fleisinger et al., 2014; Lee et al., 2012), the Reynolds Average Navier-Stokes (RANS) with turbulent closure $k$-$\omega$ Shear Stress Transport (SST) model has been used. This two-equations eddy-viscosity model has been shown to properly account for turbulence in the free stream down to the viscous sublayer level close to the turbine walls (Menter, 1993). This versatility is interesting since both turbine performances, which depend on the modeling of the boundary layers on its wall, and the wake, which is in the free stream, are of interest for this study. Regarding the $k$-$\omega$ SST model setup, the same coefficients as presented in (Menter, 1993) where used.

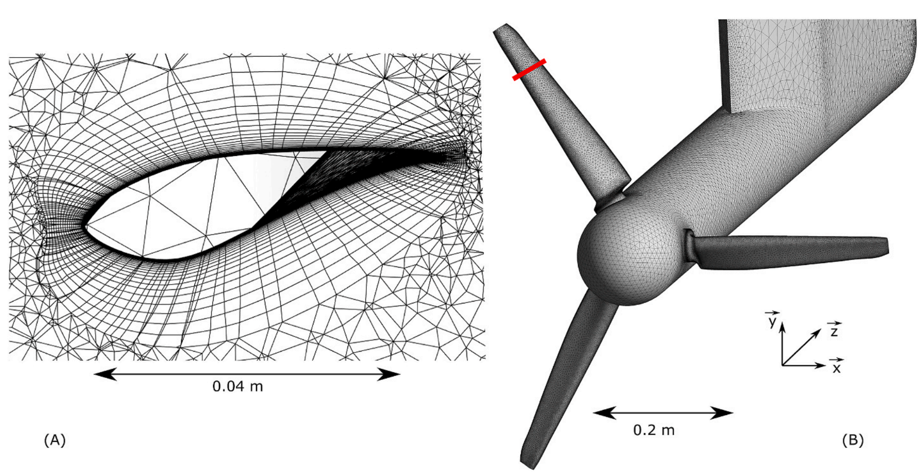


**Fig. 3.** Detailed views of the turbine mesh. View (A) shows a cross section of the mesh around one turbine blade. View (B) shows the surface mesh of the turbine and part of the nacelle. The red line shows the location of view (A) along the turbine blade. (For interpretation of the references to colour in this figure legend, the reader is referred to the Web version of this article.)

**Table 3**
Meshing parameters used for the simulations.

| Global meshing parameter | |
|---|---|
| Number of elements | 23,785,687 |
| Min element size | $2.75 \times 10^{-4}$ m |
| Max face size | 0.15 m |
| Curvature normal angle | 7.5° |
| Max wake cell size | $4.5 \times 10^{-2}$ m |
| **Boundary layer meshing parameter** | |
| Number of layers | 30 |
| Max thickness Blades | $1.5 \times 10^{-2}$ m |
| Max thickness Blades roots | $1.5 \times 10^{-2}$ m |
| Max thickness Hub | $3 \times 10^{-2}$ m |
| Max thickness Nacelle | $5 \times 10^{-2}$ m |

### 3.3. Computational mesh

The computational domain is divided into two sub-domains. A rotating sub-domain, which encloses the rotating part of the tidal turbine and a stationary one which encloses the rotating sub-domain and the nacelle. Both domains are meshed separately using the ANSYS meshing tool. An unstructured meshing method using tetrahedral elements is used. A detailed view of the turbine mesh, with a focus on the blade is given in Fig. 3. To ensure the continuity between both domains, the general grid interface (GGI) method is applied on all their shared boundaries. To achieve an accurate modeling of the wake, a cylindrical domain of refinement is added in the wake of the turbine, starting right after the center of its hub. This cylindrical domain has a diameter of $1.5D$. A picture of the meshed domain is given in Fig. 4.

Extensive work regarding mesh refinement and results validation has already been carried out on this exact turbine at the Laboratory of Applied Multiphase Thermal Engineering (LAMTE) at Dalhousie University (Currie et al., 2016; Podeur et al., 2018). The meshing process of the turbine is highly detailed in (Currie et al., 2016). In both papers, quality of the turbine mesh is assessed through validation of the numerical results with experimental data from (Doman et al., 2015). Regarding meshing of the wake, an extensive convergence study was carried out in (Osbourne et al., 2015).

Since the wake effect on a downstream turbine is the prime concern of this study and no experimental data are available to validate the numerical results, the GCI method was used to evaluate and report the numerical uncertainty. Such procedure is recommended and encouraged by the Journal of Fluids Engineering (Celik et al., 2008). The results from the GCI analysis are thoroughly presented in (Podeur et al., 2018). Detailed meshing parameters are given in Table 3.

Finally, although no experimental data are available for this turbine geometry and configuration, this RANS $k$-$\omega$ SST numerical approach has been used in a previous study by the authors (Leroux et al., 2019) where a turbine previously used for an experimental wake characterization and measurement campaign was modelled with numerical results compared to reported experimental ones from (Mycek et al., 2004). This showed that RANS $k$-$\omega$ SST slightly over predicts the velocity deficit up to $10D$ in the wake of a turbine. This would translate for this study in slightly reduced velocity on the downstream turbine blades leading to smaller absolute load amplitudes. Again, since this work aims primarily at describing an approach to extract transient and local loads on turbine blades, the numerical method was considered adequate even with this slight overprediction of velocity deficit.

### 3.4. Turbine operation

For both upstream and downstream turbines, simulations are performed at constant speed for a given tip speed ratio (TSR), given as follows:

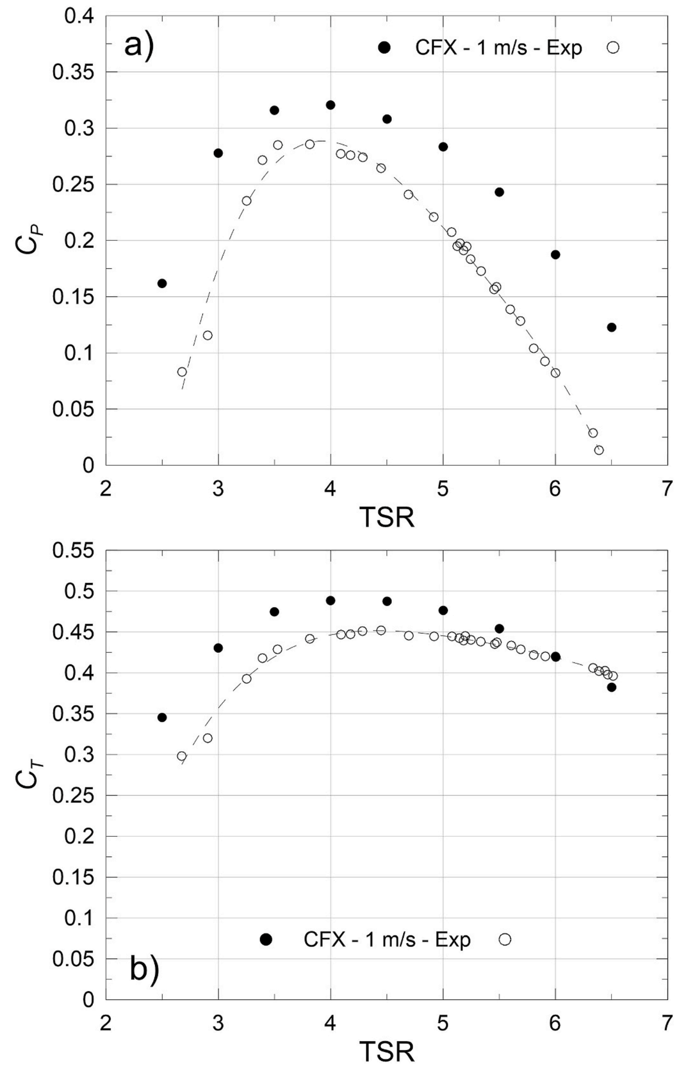


**Fig. 5.** Comparison between numerical and experimental results. a) Power coefficient $\boldsymbol{C_p v}$ ariation with respect to the TSR. b) Thrust coefficient $\boldsymbol{C_T v}$ ariation with respect to the TSR.

$$TSR = \frac{\omega D}{2U_0} \tag{1}$$

where $\omega$ is the rotational speed of the turbine and $U_0$ is the inlet velocity. In this study, $U_0$ is constant and is set to 1 m/s. To achieve the desired TSR value, the rotational velocity $\omega$ is adjusted accordingly. For both upstream and downstream turbines, their rotational speeds are equal and constant.

Results presented in this study are taken from the simulations once a quasi steady-state is reached. Transient effects during the start-up phase are not addressed. The term quasi steady-state is mainly due to the nature of the response of the downstream turbine, from its interaction with the incoming fluctuating wake flow induced by the upstream turbine. Such fluctuations may induce significant torque variations on the downstream turbine, which could lead to variations of the rotational speed with respect to the total rotational inertia of the system. However, such fluid to structure interaction requires extra information on the system design which are not available to the author. Thus, such dynamic behaviors were not considered for the simulation.

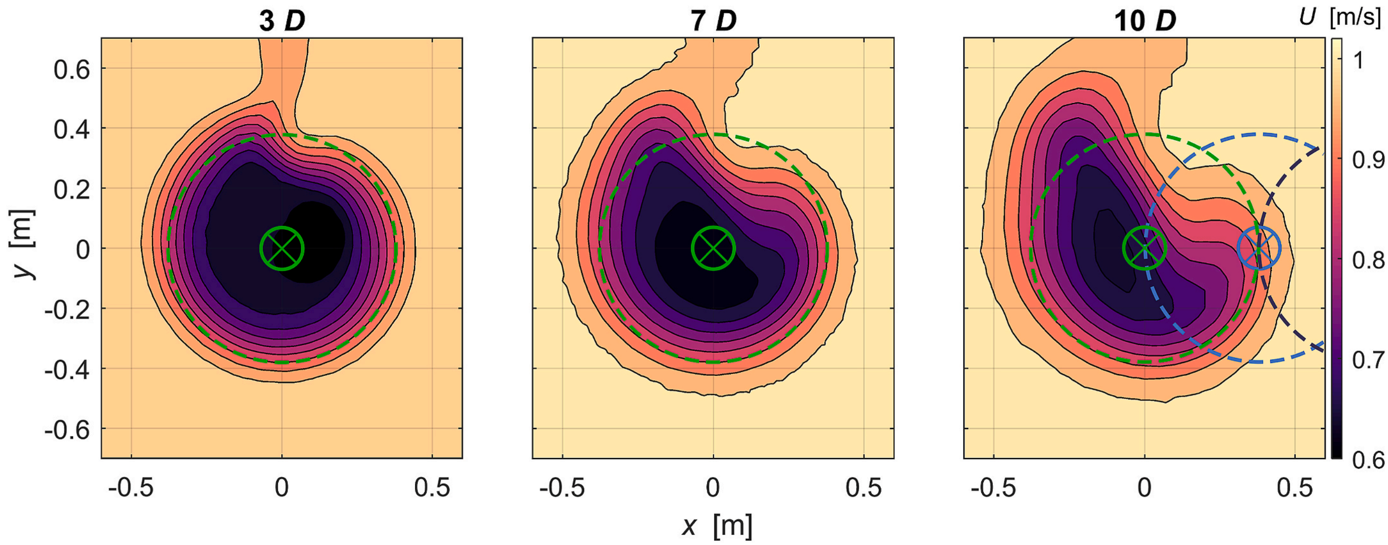


**Fig. 6.** Flow velocity within the wake. Cross-sections are located 3*D*, 7*D* and 10*D* downstream the first turbine. Both upstream and downstream turbines hub centers and swept areas are represented on the 10*D* cross section with blue and green markers respectively. (For interpretation of the references to colour in this figure legend, the reader is referred to the Web version of this article.)

### 3.5. Solver parameters

The transient simulations are performed on ANSYS CFX using a time step of 0.01 s, a total duration of 15 s (one turbine) and 20 s (two turbines). The selected time step value allows to keep the maximum Courant number value below 1 for every simulation. A high order advection scheme, which is a blend of 1st and 2nd order is used. The discretization method for the transient terms is a 2nd order backward Euler scheme. The convergence criteria are based on the residual RMS with a goal value of $10^{-5}$ and a maximum number of iterations per time step set to 10.

### 3.6. Single turbine performance and model validation

For the validation, transient simulations are performed for nine TSR values with the assessment domain mesh. The reference variables are the power and thrust coefficients $C_p$ and $C_T$, given as follows:

$$C_p = \frac{2\omega Q}{\rho A U_0^3} \tag{2}$$

$$C_T = \frac{2T}{\rho A U_0^2} \tag{3}$$

where $Q$ and $T$ are the turbine torque and thrust respectively, $\rho$ is the freshwater density taken as 997 kg/m$^3$, $\omega$ is the rotational rate in rad/s. Variable $A = 0.25\pi D^2$ is the swept area in square meters of the turbine. The total simulation length is 15 s, which is enough to reach a steady-state flow with constant $C_p$ and $C_T$ values.

The values obtained from these simulations are compared to experimental results obtained in the tow tank test, given in (Doman et al., 2015). Numerical and experimental results are shown in Fig. 5. For both $C_p$ and $C_T$, discrepancies between numerical and experimental results are observed. Even though numerical and tow tank results follow the same trend, turbine performances are slightly overestimated. For the $C_T$ values, the highest relative difference with respect to the experimental results is observed at TSR = 2.5, with a value of 34 %. The lowest relative difference is observed at TSR = 6, with a value of 1.3 %. Regarding the $C_p$ values, the relative error with respect to the experimental results are higher compared to the $C_T$ one. For TSR = 2.5, 6 and 6.5, the relative error is well above 100 %. The lowest relative error is observed at TSR = 4 with a value of 13.8 %. Regarding the measurements uncertainty presented in (Doman et al., 2015), mean relative uncertainties for $C_T$ and $C_P$ coefficients are respectively 0.85 % and 2.73 %.

These differences between numerically predicted and experimental values can be explained by several reasons. First, the rotor depth of the numerical model differs from the experimental setup. This change was made to ensure that the turbine was centered in the canal to avoid excessive interaction between the turbine wake and the ceiling of the numerical domain. Moreover, the ceiling of the numerical domain is considered to be a solid surface where it is a free surface in the case of the towing tank. The effect of the free surface deflection induced by the blade passage and the subsequent wake are thus not considered. Secondly, as demonstrated by Currie et al. (2016), simplifications during the modeling process of the turbine may have a significant influence on the predicted $C_p$ and $C_T$ values. This is especially true within the trailing edge area. Additionally, some physical phenomenon, such as hydro-mechanical interaction between the flow and blades, vibration, potential rotational speed variation and energy loss, are neglected. Furthermore, impacts of flow cavitation at high TSR are not model, which also help explains observed differences between experimental and numerical results in that region of operation.

Therefore, the values obtained can still be considered reasonably satisfactory regarding the approximation made on the turbine geometry and the grid selection made to keep the computational time reasonable. Therefore, the meshing parameters given in Table 3 are considered to be satisfactory.

## 4. Results and discussion

The results presented in this section were all obtained for TSR = 4, which corresponds to the maximum of power production of the turbine, and also a TSR within the range where the numerical validation is more accurate.

### 4.1. Turbine wake

The velocity loss within the upstream turbine wake is investigated first. In the following analysis, the wake is defined as the region where the flow velocity is smaller then the upstream inlet velocity value. Fig. 6 shows the flow velocity at cross-sections situated 3*D*, 7*D* and 10*D* in the wake of the turbine; remembering that the downstream turbine sits 10*D*

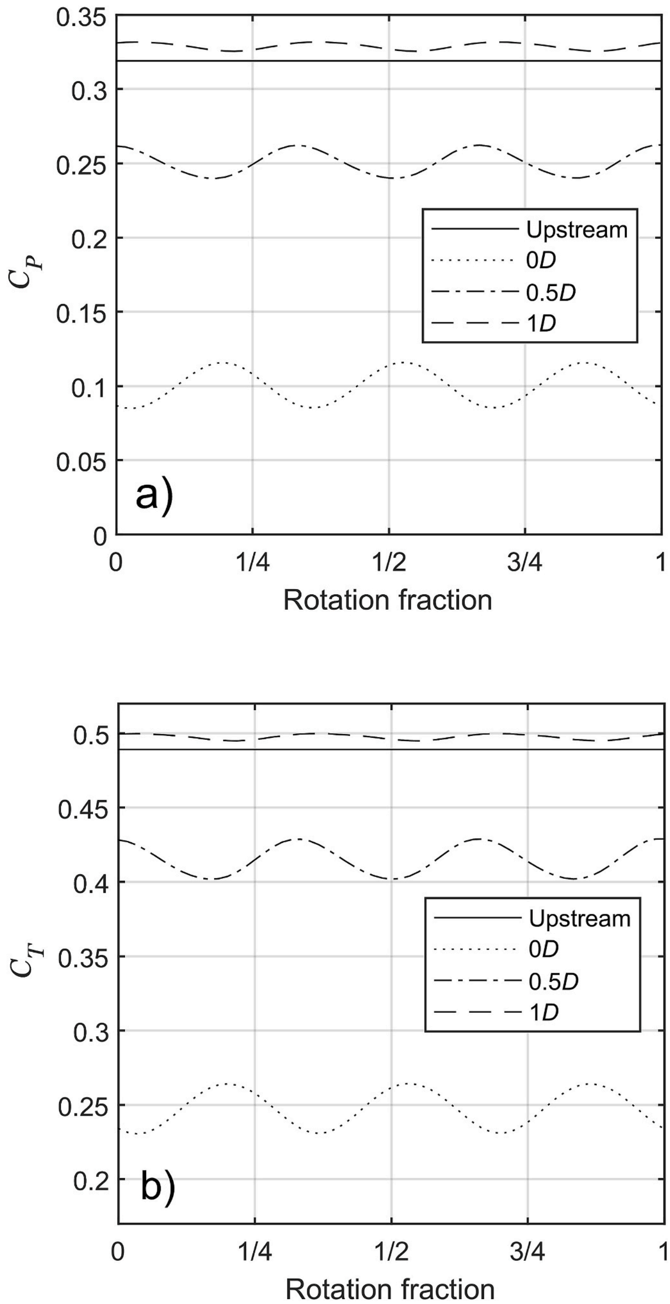


**Fig. 7.** a) Numerical $C_p$ and b) $C_T$ over one rotation period at TSR = 4 for the upstream and downstream turbines for the three offsets.

downstream of the first turbine. The swept area and the hub center of the upstream turbine are drawn in green for the 3, 7 and 10$D$ downstream locations. The swept area and the hub of the downstream turbine for the 0.5$D$ and 1$D$ offsets are drawn in blue and black for the 10$D$ location. From Fig. 6, it is clear that the flow is far from having recovered, with a minimum velocity at 10$D$ of 0.65 m/s which is 65 % of the inlet velocity. At 10$D$, the mean flow velocity within the swept area of the upstream turbine is approximately 0.75 m/s. Outside the wake, the flow velocity sees a significant increase of 10 % compared to the inlet velocity with a value of 1.1 m/s. This increase is the result of mass conservation and blockage effect, induced by the presence of the turbine and nacelle. Regarding the shape of the wake, a strong asymmetry appears while the wake is advected downstream. This is especially noticeable in the upper part of the wake at 10$D$. The origin of this asymmetry can be attributed to the wake interaction with the nacelle.

**Table 4**
Upstream and downstream turbine performances.

| | Upstream turbine | Downstream turbine Offsets | | |
|---|---|---|---|---|
| | | 0$D$ | 0.5$D$ | 1$D$ |
| $C_p$ mean | 0.3190 | 0.1004 | 0.2507 | 0.3288 |
| Amplitude | – | 0.0309 | 0.0230 | 0.0063 |
| Relative amplitude | – | 30.77 % | 9.17 % | 1.91 % |
| $C_T$ mean | 0.4890 | 0.2478 | 0.4150 | 0.4975 |
| Amplitude | – | 0.0339 | 0.0280 | 0.0049 |
| Relative amplitude | – | 13.68 % | 6.74 % | 0.98 % |

### 4.2. Downstream turbine performances

The power and thrust coefficients $C_p$ and $C_T$ are evaluated when the quasi steady-state phase of the simulation is reached. This phase consists of the last 10 turbine rotations over a total of 33. Time evolution of both coefficients for the upstream and downstream turbine, for all three offset positions over one full rotation period, is given in Fig. 7. These results show the oscillatory nature of the downstream turbine performances. Over 10 rotations, the average $C_p$ and $C_T$ values are computed and both amplitude and relative amplitude with respect to the mean value of the signal are evaluated. The obtained results are presented in Table 4.

Foremost, it appears that the introduction of a downstream turbine has little to no effects on the upstream turbine performances, with means $C_p$ and $C_T$ values almost identical to what is obtained with the single turbine assessment domain. The relative difference with respect to the single turbine results are 0.50 % for $C_p$ and 0.08 % for $C_T$. These observations are in line with what was observed in (Jeffcoate et al., 2016). From Table 4, the 0$D$ configuration gives the lowest performance, followed by the 0.5$D$ and 1$D$ offsets. This is explained by the fact that with a 0$D$ offset, the downstream turbine sees a highly turbulent flow which already has a rotational component with a high level of velocity deficit. The average velocity encountered by the turbine in the 0$D$ configuration is approximately 20–25 % lower than the inlet velocity. This clearly explains why the predicted $C_p$ is 69 % lower than the upstream turbine value. This velocity reduction decreases to 21 % for the 0.5$D$ offset configuration and a slight increase of 3 % in $C_p$ is observed when the downstream turbine is offset by 1$D$. For $C_T$, the 0$D$ configuration shows a reduction of 49 % compared to the upstream turbine. The 0.5$D$ configuration shows only a reduction of 15 % while for 1$D$, $C_T$ increases slightly by 2 %. The increase of performance displayed in the 1$D$ configuration is explained by the slight increase of the flow velocity outside the wake, as mentioned in the previous section.

Regarding the oscillatory behavior of the downstream turbine performances, it appears that the amplitudes of the oscillations is significantly affected by the lateral offset configuration of the downstream turbine. The highest relative amplitudes of the $C_p$ and $C_T$ signals with respect to the mean values are observed for the 0$D$ configuration, with values of 30.77 % and 13.68 % for $C_p$ and $C_T$ respectively. The lowest relative amplitude is observed for the 1$D$ configuration with values of 1.91 % and 0.98 % for $C_p$ and $C_T$ respectively. Each time series display the same characteristics, with an oscillation period equal to 1/3rd of the rotation period of the turbine; although the three signals are out of phase. This is the result of the turbine blades experiencing different incoming flows depending on the turbine lateral offset. The intensity of the time varying component of the incoming flow velocity in the wake is negligible compared to the local mean flow velocity and has no significant effect on the downstream turbine performances variations.

These variations observed for the turbine performances are happening rapidly on a time scale equal to 1/3rd of the rotation period, which is less than 0.2 s for a TSR = 4 and $U_0 = 1$ m/s. Such rapid variations can potentially create mechanical issues within the various rotating parts and the generator. More importantly, from the loading/structural aspect of the blades, $C_T$ sees fluctuations up to 13.68 % around

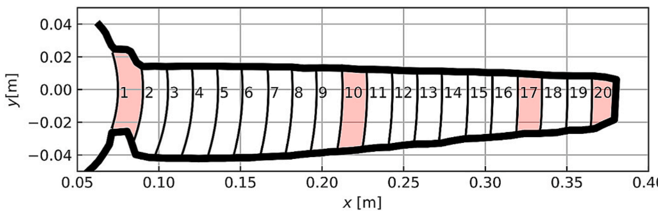


**Fig. 8.** Turbine blade sections for discrete loading evaluation. The sections of interest in the rest of the study are highlighted in red. (For interpretation of the references to colour in this figure legend, the reader is referred to the Web version of this article.)

**Table 5**
Blade section areas.

| Section | $A_s$ [m$^2$] | Section | $A_s$ [m$^2$] |
|---|---|---|---|
| 1 | $2.55 \times 10^{-3}$ | 11 | $1.57 \times 10^{-3}$ |
| 2 | $2.05 \times 10^{-3}$ | 12 | $1.52 \times 10^{-3}$ |
| 3 | $2.03 \times 10^{-3}$ | 13 | $1.44 \times 10^{-3}$ |
| 4 | $2.00 \times 10^{-3}$ | 14 | $1.39 \times 10^{-3}$ |
| 5 | $1.95 \times 10^{-3}$ | 15 | $1.30 \times 10^{-3}$ |
| 6 | $1.90 \times 10^{-3}$ | 16 | $1.24 \times 10^{-3}$ |
| 7 | $1.82 \times 10^{-3}$ | 17 | $1.18 \times 10^{-3}$ |
| 8 | $1.77 \times 10^{-3}$ | 18 | $1.13 \times 10^{-3}$ |
| 9 | $1.73 \times 10^{-3}$ | 19 | $1.09 \times 10^{-3}$ |
| 10 | $1.63 \times 10^{-3}$ | 20 | $1.01 \times 10^{-3}$ |

the average load, this will lead to cyclical and rapid load variations on the turbine blades. From a designer point of view, the results provided by these simulations are invaluable information to determine the extent of the loads, and fluctuation of those loads, on the turbine blades of the downstream turbine over time.

### 4.3. Downstream turbine blade loading analysis

In order to evaluate the hydrodynamic load along the blade span with respect to the blade location, the local thrust coefficient $C_{Tl}$ is computed for each blade over a finite number of sections. The sections considered for this study are given in Fig. 8. Their respective areas are given in Table 5. The local thrust coefficient is computed as follows:

$$C_{Tl} = \frac{2T_l}{\rho A_s U_0^2} \tag{4}$$

where $T_l$ is the local thrust computed at the $n$th section and $A_s$ is the total area of the $n$th section.

From the hydrodynamic load, the flap-wise root bending moment coefficient $C_M$ is computed as follows:

$$C_M = \frac{2M}{\rho A_b R U_0^2} \tag{5}$$

where $M$ is the flap-wise root bending moment acting on the blade root and $A_b$ is the single blade surface area, which is equal to 0.0323 m$^2$.

First, focus is made on the time variation of the local thrust coefficient for several sections along the blade. Sections 1, 10, 17 and 20 are of interest and are highlighted in red on Fig. 8. The variation of $C_{Tl}$ with respect to time for these sections and all three turbine offsets, are given in Fig. 9. Regarding the blade load distribution, the results display the classical load distribution for a hydrofoil, with an increase from the root (section 1) to 2/3rd of the blade (sections 10 and 17) and a decrease toward the tip (section 20). The 0$D$ offset results display the most complex signal with a higher number of oscillations. The 0.5$D$ offset results display a much simpler signal compared to the 0$D$ offset. Regarding the amplitudes of the signals, the same order of magnitude can be observed for all four sections for both 0.5$D$ and 0$D$ offsets. The 1$D$ offset results show a much smaller amplitude, which is 8 times smaller compared to the amplitude observed for the two other offsets.

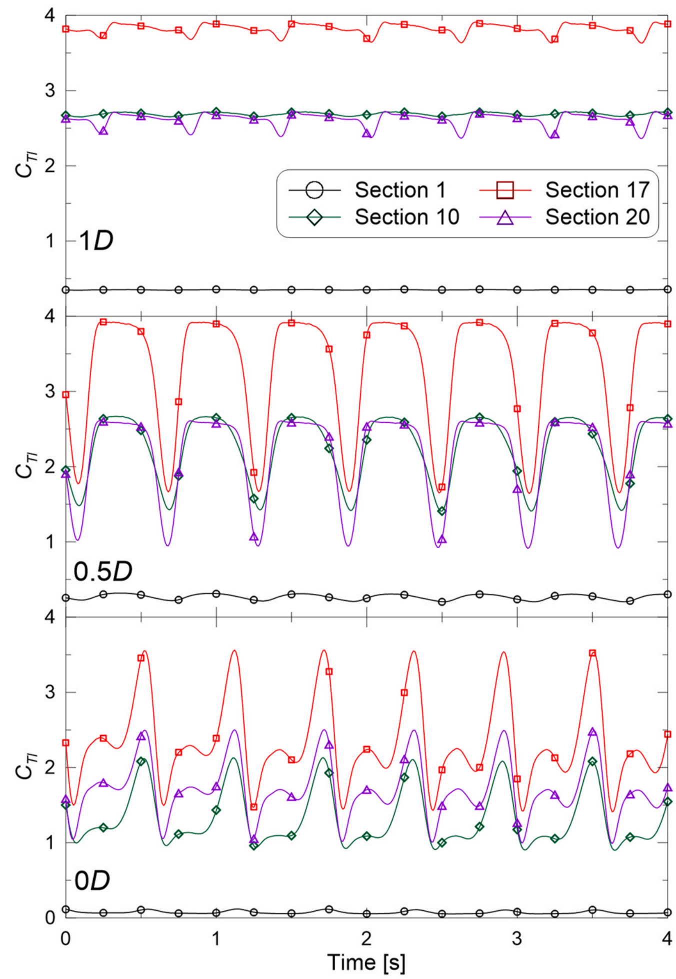


**Fig. 9.** Time evolution of local thrust coefficient $C_{Tl}$ for 4 blade sections over 4 s. The results are given for all three turbine offsets with 1$D$, 0.5$D$ and 0$D$ from top to bottom.

To further understand the signals shown in Fig. 9, a phase averaging is performed and the results are plotted in Fig. 10, where the mean periodic signal is surrounded by a grey area which represents the standard deviation. As presented in (Bergami and Gaunaa, 2014), the mean signal represents the deterministic load that occurs periodically and the standard deviation represents the stochastic load induced by the presence of turbulence within the flow. From Fig. 10, it appears that the stochastic load drops significantly when the turbine offset goes from 0$D$ to 0.5$D$ and is marginal for the 1$D$ offset.

Secondly, the blade load distribution over the swept area is considered. The local thrust coefficients $C_{Tl}$, computed over 1300 time-steps for all three turbine configurations, were analysed using MatLab. The results are ordered with respect to the blade location on the swept area and are distributed over 72 sectors of 5° each. This leads to an average of 34 $C_{Tl}$ values per blade section, per sector. From these results, the mean value of $C_{Tl}$ and the associated $CV$ (coefficient of variation), which is the standard deviation of the series divided by its mean and expressed as a percentage, are computed. The results for $C_{Tl}$ values are given in Fig. 11 and resulting $CV$ values are presented in Fig. 12.

Regarding the $C_{Tl}$ distribution, the results are in line with the observation made earlier about the global performances. The 0$D$ setup shows the most non-uniform blade load distribution. The most dramatic changes occur for the blade sections ranging from 10 to 20 (half of the blade next to the tip) where the highest amplitude between the maximum and the minimum load for the same span location is observed.

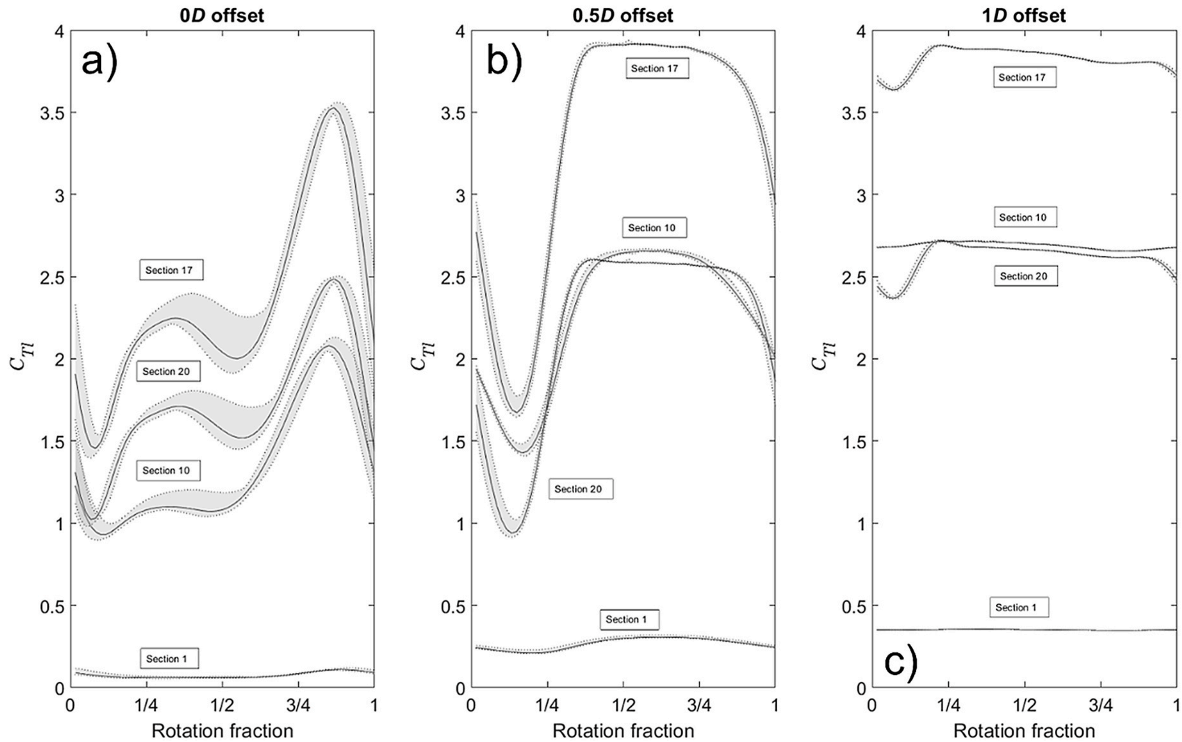


**Fig. 10.** Phase averaging of the local thrust coefficient $C_{Tl}$ for 4 blade sections over one turbine rotation. The results are given for all three turbine offsets with 0*D*, 0.5*D* and 1*D* from left to right. The mean signal is displayed in solid line while the standard deviation is displayed as a grey area surrounding the mean signal.

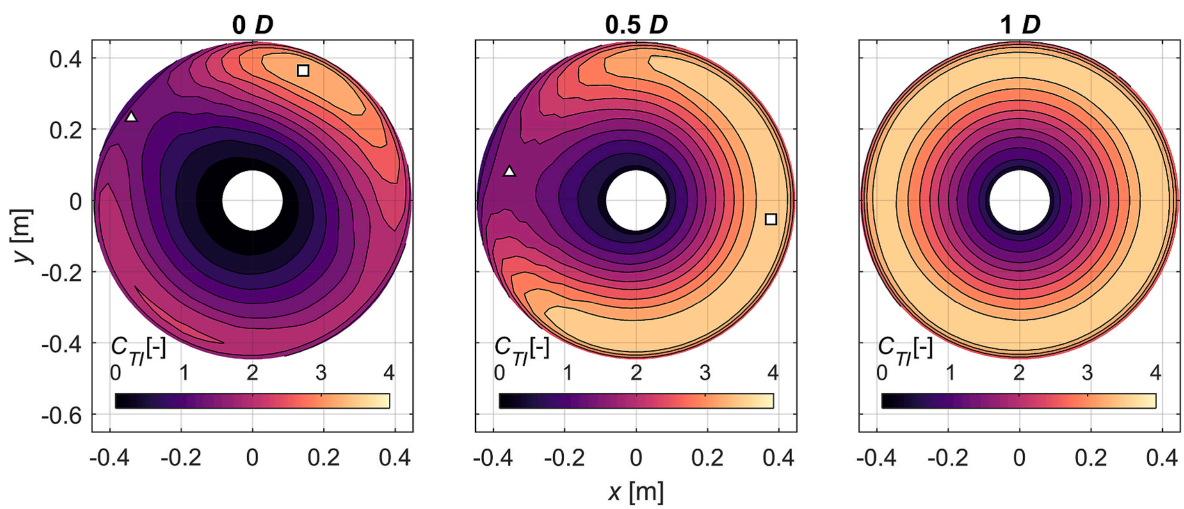


**Fig. 11.** Mean $C_{Tl}$ values distribution over the swept area for all three offsets.

The maximum $C_{Tl}$ is observed around section 18 with a value of 3.52. The $C_{Tl}$ value drops to a minimum of 1.42 for the same blade section later in its rotation. These maximum and minimum are indicated in Fig. 11 by a square and a triangular marker respectively. Therefore, the load on the same blade section will change by a factor of 2 between maximum and minimum.

For the 0.5*D* setup, the blades see less asymmetry and an overall higher $C_{Tl}$ value. The blade load distribution is fairly constant over half of the swept area and sees a progressive decrease and increase on the West/Northwest sector when the blades rotate through the largest component of the upstream turbine wake. The maximum $C_{Tl}$ value is 3.82, indicated by a square marker, while the lowest $C_{Tl}$ value for the same span location is equal to 1.7 and is indicated by a triangle marker. The 1*D* setup experiences almost no asymmetry regarding the $C_{Tl}$ distribution. The only marginal variations are taking place near section 20 and are barely noticeable.

Regarding the *CV* distribution in Fig. 12, the 0*D* setup experiences the strongest variability with the bulk of the variation located in the North/West sector of the swept area. The maximum value of *CV* is 13.3 % and is located near the turbine hub. To a lesser extent, a reasonable amount of variation, with a value of *CV* between 3 % and 6 % can also be observed in the South-Southeast region of the swept area around sections 15 to 20. These areas roughly correspond to the ones where lower value of $C_{Tl}$ are observed. For the 0.5*D* setup, the South/West sector of the swept area is the one which presents the highest values of *CV* with a maximum of 6.7 % around sections 19 and 20. The upper left quarter of the swept area is also subject to some variation but to a lower level, with *CV* values ranging from 2.5 % to 4.5 % between sections 15 to 20. For the

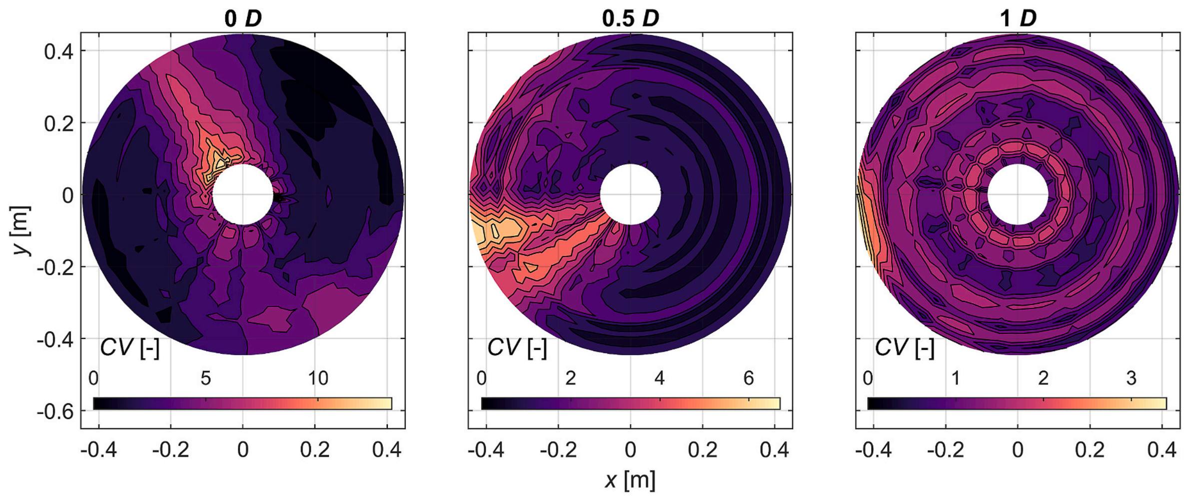


**Fig. 12.** Mean *CV* values distribution over the swept area for all three offsets.

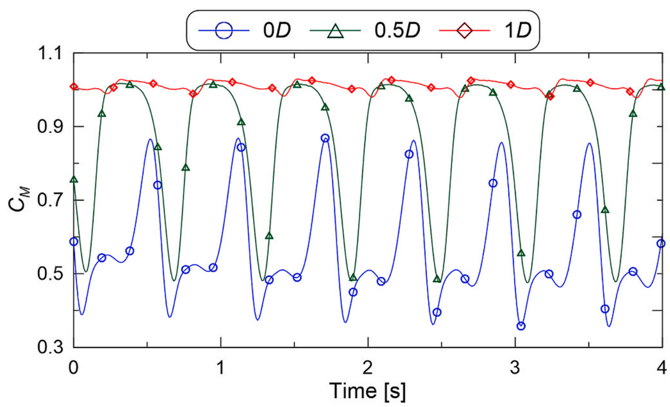


**Fig. 13.** Time evolution of the flap-wise root bending moment coefficient $C_M$ over 4 s. The results are given for all three turbine offsets.

1*D* setup, as expected, very small variations are observed, with the vast majority of the swept area having a *CV* value below 2 %. The highest variation is observed for the West/Southwest sector around sections 19 and 20, where the *CV* reaches 3.4 %.

Finally, attention is drawn to the time variation of flap-wise root bending moment coefficient $C_M$. The variation of the $C_M$ with respect to time for these sections and for all three turbine offsets are given in Fig. 13. Similarly to what is observed for the $C_{Tl}$ values in Fig. 9, The 0*D* offset results display the most complex signal with a higher number of oscillations. The 0.5*D* offset results display a much simpler signal compared to the 0*D* offset. Regarding the amplitude of the signals, the same order of magnitude can be observed for all four blade sections for both 0.5*D* and 0*D* offsets. The 1*D* offset results show a much smaller amplitude, which is 12 times smaller compared to the amplitude observed for the two other offsets. A phase averaging is performed on these signals and the results are plotted in Fig. 14. As with the $C_{Tl}$ values in Fig. 10, the 0*D* offset gives the signal with the highest variability, whereas the variability is negligible for the 0.5*D* and 1*D* offsets. Compared to the results in Fig. 10, the stochastic effect on the flapwise bending moment is of lesser intensity. This is due to the flap-wise root bending moment coefficient $C_M$ being an integral value, which smooths the signal by summing all the sections contributions.

## 5. Conclusion

A fully transient numerical model of two three-bladed horizontal axis tidal turbines positioned one behind the other with a clearance of 10*D* has been created and simulated with a primary objective of developing an approach to extract CFD data in order to determine transient and local blade loading. For a constant inlet velocity of 1 m/s, the results show that at a distance of 10*D* behind the turbine, the wake still shows large areas of velocity deficit, up to 35 % in velocity reduction compared to the inlet free-stream velocity. The wake also shows a large degree of asymmetry which will impact the overall performances of a second turbine downstream at this position.

When looking at the behavior of a downstream turbine, it was found that $C_P$ and $C_T$ were both reduced, by up to 69 % and 49 % respectively when the downstream turbine is offset transversely by less than a full turbine diameter. Both power and thrust are then subjected to large and rapid fluctuations which have an impact on energy harvesting and overall blade loading cycling leading to fatigue issues.

Looking specifically at the loading on the blades, a method was presented where the length of each blade was split in 20 smaller sections, on which acting forces were calculated at each instant in time. This resulted in determination of forces acting locally on each blade section that varied, sometimes greatly, with time. This variation over time coming from two sources: i) the local variation of the flow in the wake of the first turbine over time, and ii) the blade itself rotating over time and seeing different regions of the wake. The combination of these two sources resulted in local forces that varied rotation after rotation following a similar variation pattern, but the variability in the wake itself also resulted in variations from this main pattern from one rotation to the next. For example, significant fluctuation of the blade load is observed for the 0*D* and 0.5*D* offsets, with a signal amplitude 8 times greater to what is observed for the 1*D* offset. Furthermore, over one turbine rotation, the load can vary by a factor of up to 2 during the blade rotation and changes in the amplitude of the load applied along the blade can fluctuate by more than 13 %. Regarding the flap-wise root bending moment, the amplitude of the signal for the 0*D* and the 0.5*D* offsets is 12 time higher to what is observed for the 1*D* offset.

This work shows that the approach used to extract the required information from CFD results to compute transient and local loads on blades works. Future work will focus on more expensive, but more accurate turbulence modelling of the wake (DES to start) used in combination with this transient and local load extraction approach, to gain deeper insight on the variability and cyclability of the forces on blades. The ultimate goal being to assist designers in recognize how fatigue will set in blades based on these transient and local loads.

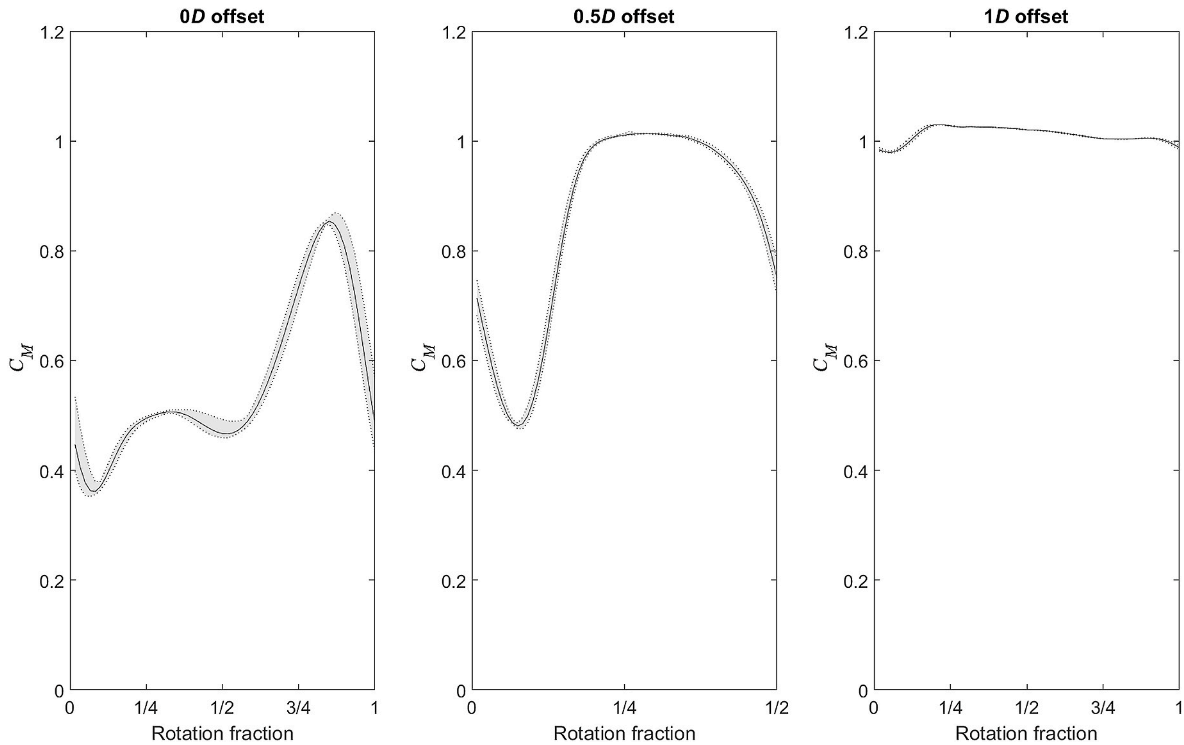


**Fig. 14.** Phase averaging of flap-wise root bending moment coefficient $C_M$ over one turbine rotation. The results are given for all three turbine offsets with 0*D*, 0.5*D* and 1*D* from left to right. The mean signal is displayed in solid line while the standard deviation $\sigma$ is displayed as a grey area surrounding the mean signal.

## CRediT authorship contribution statement

**Vincent Podeur:** Writing – original draft, Visualization, Validation, Software, Methodology, Investigation, Formal analysis, Data curation, Conceptualization. **Lise Michaud:** Writing – review & editing, Visualization, Validation, Software, Investigation. **Dominic Groulx:** Writing – review & editing, Supervision, Project administration, Methodology, Funding acquisition, Conceptualization. **Christian Jochum:** Writing – review & editing, Supervision, Funding acquisition, Conceptualization.

## Declaration of competing interest

The authors declare that they have no known competing financial interests or personal relationships that could have appeared to influence the work reported in this paper.

## Acknowledgment

The authors are thankful to the French Embassy in Canada for the France Canada Research Fund (FCRF) award that supported this work, as well as to the Canadian Foundation for Innovation (CFI) for their financial assistance regarding the computing systems and the Faculty of Engineering at Dalhousie University.

## References

Afgan, I., McNaughton, J., Rolfo, S., Apsley, D., Stallard, T., Stansby, P., 2013. Turbulent flow and loading on a tidal stream turbine by les and rans. Int. J. Heat Fluid Flow 43, 96–108.

Ahmed, U., Apsley, D., Afgan, I., Stallard, T., Stansby, P., 2017. Fluctuating loads on a tidal turbine due to velocity shear and turbulence: comparison of cfd with field data. Renew. Energy 112, 235–246.

Allmark, M., Ellis, R., Ebdon, T., Lloyd, C., Ordonez-Sanchez, S., Martinez, R., Mason-Jones, A., Johnstone, C., O'Doherty, T., 2021. A detailed study of tidal turbine power production and dynamic loading under grid generated turbulence and turbine wake operation. Renew. Energy 169, 1422–1439.

Badshah, M., VanZwieten, J., Badshah, S., Jan, S., 2019. CFD study of blockage ratio and boundary proximity effects on the performance of a tidal turbine. IET Renew. Power Gener. 13, 744–749.

Bai, G., Li, J., Fan, P., Li, G., 2013. Numerical investigations of the effects of different arrays on power extractions of horizontal axis tidal current turbines. Renew. Energy 53, 180–186.

Bergami, L., Gaunaa, M., 2014. Analysis of aeroelastic loads and their contributions to fatigue damage. In: Journal of Physics: Conference Series, vol. 555. IOP Publishing, 012007.

Blackmore, T., Myers, L.E., Bahaj, A.S., 2016. Effects of turbulence on tidal turbines: implications to performance, blade loads, and condition monitoring. International Journal of Marine Energy 14, 1–26.

Celik, I.B., Ghia, U., Roache, P.J., Freitas, C.J., 2008. Procedure for estimation and reporting of uncertainty due to discretization in CFD applications. Journal of fluids Engineering-Transactions of the ASME 130, 078001.

Currie, G., Osbourne, N., Groulx, D., 2016. Numerical modelling of a three-bladed NREL S814 tidal turbine. In: Proceedings of the Third. Asian Wave and Tidal Energy Conference, p. 10.

Doman, D.A., Murray, R.E., Pegg, M.J., Gracie, K., Johnstone, C.M., Nevalainen, T., 2015. Tow-tank testing of a 1/20th scale horizontal axis tidal turbine with uncertainty analysis. International Journal of Marine Energy 11, 105–119.

du Feu, R., Funke, S., Kramer, S., Hill, J., Piggott, M., 2019. The trade-off between tidal-turbine array yield and environmental impact: a habitat suitability modelling approach. Renew. Energy 143, 390–403.

Fairley, I., Masters, I., Karunarathna, H., 2015. The cumulative impact of tidal stream turbine arrays on sediment transport in the pentland firth. Renew. Energy 80, 755–769.

Finnegan, W., Fagan, E., Flanagan, T., Doyle, A., Goggins, J., 2020. Operational fatigue loading on tidal turbine blades using computational fluid dynamics. Renew. Energy 152, 430–440.

Fleisinger, M., Vesenjak, M., Hriberšek, M., 2014. Flow driven analysis of a darrieus water turbine. Strojniški vestnik-Journal of Mechanical Engineering 60, 769–776.

Gajardo, D., Escauriaza, C., Ingram, D.M., 2019. Capturing the development and interactions of wakes in tidal turbine arrays using a coupled bem-des model. Ocean Eng. 181, 71–88.

Guy, C., Hart, E., Vengatesan, V., Forehand, D., 2024. Numerical modelling of a 1.5 MW tidal turbine in realistic coupled wave–current sea states for the assessment of turbine hub-depth impacts on mechanical loads. Ocean Eng. 292, 116577.

Hammar, L., Andersson, S., Eggertsen, L., Haglund, J., Gullström, M., Ehnberg, J., Molander, S., 2013. Hydrokinetic turbine effects on fish swimming behaviour. PLoS One 8, e84141.

Jeffcoate, P., Whittaker, T., Boake, C., Elsaesser, B., 2016. Field tests of multiple 1/10 scale tidal turbines in steady flows. Renew. Energy 87, 240–252.

Lam, R., Dubon, S.L., Sellar, B., Vogel, C., Davey, T., Steynor, J., 2023. Temporal and spatial characterisation of tidal blade load variation for structural fatigue testing. Renew. Energy 208, 665–678.

Lee, J.H., Park, S., Kim, D.H., Rhee, S.H., Kim, M.-C., 2012. Computational methods for performance analysis of horizontal axis tidal stream turbines. Appl. Energy 98, 512–523.
Leroux, T., Osbourne, N., McMillan, J., Groulx, D., Hay, A., 2016. Numerical modelling of a tidal turbine behaviour under realistic unsteady tidal flow. In: Proc. of Asian Wave and Tidal Energy Conference, p. 10.
Leroux, T., Osbourne, N., Groulx, D., 2019. Numerical study into horizontal tidal turbine wake velocity deficit: Quasi-steady state and transient approaches. Ocean Eng. 181, 240–251.
Liu, H., Li, Y., Lin, Y., Li, W., Gu, Y., 2020. Load reduction for two-bladed horizontal-axis tidal current turbines based on individual pitch control. Ocean Eng. 207, 107183.
Lloyd, C., Allmark, M., Ordonez-Sanchez, S., Martinez, R., Johnstone, C., Germain, G., Gaurier, B., Mason-Jones, A., O'Doherty, T., 2021. Validation of the dynamic load characteristics on a tidal stream turbine when subjected to wave and current interaction. Ocean Eng. 222, 108360.
Magnier, M., Delette, N., Druault, P., Gaurier, B., Germain, G., 2022. Experimental study of the shear flow effect on tidal turbine blade loading variation. Renew. Energy 193, 744–757.
Marsh, P., Penesis, I., Nader, J.-R., Couzi, C., Cossu, R., 2021. Assessment of tidal current resources in clarence strait, Australia including turbine extraction effects. Renew. Energy 179, 150–162.
Masters, I., Malki, R., Williams, A.J., Croft, T.N., 2013. The influence of flow acceleration on tidal stream turbine wake dynamics: a numerical study using a coupled bem–cfd model. Appl. Math. Model. 37, 7905–7918.
Menter, F., 1993. Zonal two equation kw turbulence models for aerodynamic flows. In: 23rd Fluid Dynamics, Plasmadynamics, and Lasers Conference, p. 2906.
Milne, I., Day, A., Sharma, R., Flay, R., 2015. Blade loading on tidal turbines for uniform unsteady flow. Renew. Energy 77, 338–350.
Munaweera Thanthirige, T.R., Goggins, J., Flanagan, M., Finnegan, W., 2023. A state-of-the-art review of structural testing of tidal turbine blades. Energies 16 (10), 4061.
Mycek, P., Gaurier, B., Germain, G., Pinon, G., Rivoalen, E., 2004. Experimental study of the turbulence intensity effects on marine current turbines bahviour. Part I: one single turbine. Renew. Energy 66, 729–746.
Mycek, P., Gaurier, B., Germain, G., Pinon, G., Rivoalen, E., 2014. Experimental study of the turbulence intensity effects on marine current turbines behaviour. Part II: two interacting turbines. Renew. Energy 68, 876–892.
Myers, L., Bahaj, A., 2012. An experimental investigation simulating flow effects in first generation marine current energy converter arrays. Renew. Energy 37 (1), 28–36.
Nevalainen, T., Johnstone, C., Grant, A., 2016. A sensitivity analysis on tidal stream turbine loads caused by operational, geometric design and inflow parameters. International Journal of Marine Energy 16, 51–64.
Onoufriou, J., Russell, D.J., Thompson, D., Moss, S.E., Hastie, G.D., 2021. Quantifying the effects of tidal turbine array operations on the distribution of marine mammals: implications for collision risk. Renew. Energy 180, 157–165.
Osbourne, N., 2015. 3D Modelling of a Tidal Turbine – a Numerical Investigation of Wake Phenomena. Dalhousie University, Halifax, p. 114. MASc Thesis.
Osbourne, N., Groulx, D., Penesis, I., 2015. 3D modelling of a tidal turbine-an investigation of wake phenomena. In: 11th European Wave and Tidal Energy Conference. EWTEC), p. 10.
Ouro, P., Ramírez, L., Harrold, M., 2019. Analysis of array spacing on tidal stream turbine farm performance using large-eddy simulation. J. Fluid Struct. 91, 102732.
Patel, M.D., 2024. The Impact of real-world Constraints on Tidal Stream Energy Resource Assessments. University of Oxford. Doctoral dissertation.
Payne, G.S., Stallard, T., Martinez, R., Bruce, T., 2018. Variation of loads on a three-bladed horizontal axis tidal turbine with frequency and blade position. J. Fluid Struct. 83, 156–170.
Podeur, V., Groulx, D., Jochum, C., 2018. Tidal turbine interaction effect of upstream turbine wake on downstream turbine. In: Proceedings of the 4th Asian Wave and Tidal Energy Conference. AWTEC), Taipei, Taiwan, p. 10.
Porter, K.E., Ordonez-Sanchez, S.E., Murray, R.E., Allmark, M., Johnstone, C.M., O'Doherty, T., Mason-Jones, A., Doman, D.A., Pegg, M.J., 2020. Flume testing of passively adaptive composite tidal turbine blades under combined wave and current loading. J. Fluid Struct. 93, 102825.
Roc, T., Greaves, D., Conley, D.C., Leybourne, M., 2013. Optimising commercial-scale tec arrays: genetic algorithm, fractal & eco-mimicry. In: Proceedings of the 10th European Wave and Tidal Energy Conference, p. 12.
Tatum, S., Frost, C., Allmark, M., O'doherty, D., Mason-Jones, A., Prickett, P., Grosvenor, R., Byrne, C., O'Doherty, T., 2016. Wave–current interaction effects on tidal stream turbine performance and loading characteristics. International Journal of Marine Energy 14, 161–179.
Togneri, M., Pinon, G., Carlier, C., Bex, C.C., Masters, I., 2020. Comparison of synthetic turbulence approaches for blade element momentum theory prediction of tidal turbine performance and loads. Renew. Energy 145, 408–418.
Topper, M.B., Olson, S.S., Roberts, J.D., 2021. On the benefits of negative hydrodynamic interactions in small tidal energy arrays. Appl. Energy 297, 117091.
Turnock, S.R., Phillips, A.B., Banks, J., Nicholls-Lee, R., 2011. Modelling tidal current turbine wakes using a coupled rans-bemt approach as a tool for analysing power capture of arrays of turbines. Ocean Eng. 38, 1300–1307.
Zhang, J., Zhang, C., Angeloudis, A., Kramer, S.C., He, R., Piggott, M.D., 2022. Interactions between tidal stream turbine arrays and their hydrodynamic impact around Zhoushan island, China. Ocean Eng. 246, 110431.
Zhang, Z., Zhang, Y., Zheng, Y., Zhang, J., Fernandez-Rodriguez, E., Zang, W., Ji, R., 2023. Power fluctuation and wake characteristics of tidal stream turbine subjected to wave and current interaction. Energy 264, 126185.